Materials Today Communications 35 (2023) 106406

Contents lists available at ScienceDirect

Materials Today Communications

journal homepage: www.elsevier.com/locate/mtcomm

Effect of nickel and rGO on the photocatalytic properties of $Co_{3-x}Ni_xO_4$ prepared with citric acid and CTAB

Leydi Julieta Cardenas Flechas [a,b,*], Elena Xuriguera Martín [c], Jose Antonio Padilla Sanchez [c], Josep Ma. Chimenos Ribera [c], Miryam Rincón Joya [d]

[a] Facultad de Ingeniería-Departamento de Ingeniería mecánica y mecatrónica, Universidad Nacional de Colombia-sede Bogotá, Colombia
[b] Departamento de Ingeniería mecánica y mecatrónica, Fundación Universidad de América, Bogotá, Colombia
[c] Departament de Ciència de Materials i Química Física, Universitat de Barcelona, Barcelona, España
[d] Departamento de Física, Universidad Nacional de Colombia-sede Bogotá, Colombia

ARTICLE INFO

Keywords:
Co_3O_4 surfactant
Morphology
Spinel
$NiCo_3O_4$ + rGO
Photocatalytic

ABSTRACT

This work summarizes the research about $Co_{3-x}Ni_xO_4$ x = 0.0 (0%), 0.01 (1%), and 0.04 (4%) conducted with the addition of reduced graphene oxide, rGO, using two routes: with citric acid R_1 ($C_6H_8O_7$, CA) and cetyltrimethylammonium R_2 ($C_{19}H_{42}BrN$, CTAB) by sol-gel technique. The results show that the composite material —with rGO— enhanced the photocatalytic degradation of methylene blue (MB). According to the results, incorporating rGO into samples with low Ni concentrations of 1% and 4% and processed at 400 °C with R1, significantly increased their specific surface area to 31.372 $m^2.g^{-1}$ and 84.743 $m^2.g^{-1}$, respectively. The XRD technique shows the formation of pure cobalt spinel without associated secondary phases and with complete insertion of Ni into the structure. The presence of CA allows the formation of the oxide at lower temperatures. The results of the magnetic tests suggest that the samples obtained by the two synthesis routes present a paramagnetic behavior. The use of CTAB permits the formation of nanoparticles with low agglomeration. TEM images indicate that the sizes of the nanoparticles obtained in the synthesis are less than 20 nm. Thus, based on Raman spectroscopy, the vibrational modes corresponding to the $Co_{3-x}Ni_xO_4$ structure were studied, identifying a broadening and displacement of the peaks with the addition of Ni.

Moreover, the disappearance of the peaks corresponding to rGO and attributed to the coating of $Co_{3-x}Ni_xO_4$ graphene nanoparticles was observed. The adsorption isotherms show the behavior of a mesoporous textured material. The diffuse reflectance indicates that R_2 with a 1.72 eV value obtained the material with the smallest gap. In addition, the process identified that the existence of reduced graphene oxide increases the material's specific surface area, which plays a crucial role in MB degradation, outperforming the 4% Ni sample that degraded 39.65% in a two-hour treatment.

1. Introduction

The different cobalt and nickel precursors and additives have been used for the controlled synthesis of high purity materials with different shapes and sizes. Many nanostructures can be subjected to this process using cetyltrimethylammonium bromide ($C_{19}H_{42}BrN$, CTAB) as a cationic surfactant [1]. Transition metal oxide nanomaterials have been synthesized using CTAB as a cationic surfactant to control their morphology and microstructure [2]. Several researches have shown that this surfactant also plays a substantial role in the growth and nucleation of spinels, binary and ternary composites, among others [3,4], allowing the formation of new mesoporous composites [5] and the synthesis of Co_3O_4 nanoparticles [6].

On the one hand, according to Niu et al. [7], CTAB would play a decisive role in structural support and pore formation in TiO_2 performance with potential application in photocatalysis through specific surface area enhancement. Properties such as improved electrochemical performance and efficiency can be achieved using CTAB as a precursor [8]. On the other hand, complexing agents, such as citric acid, are often used to synthesize fuel compounds due to their ability to chelate metal ions and facilitate the formation of highly pure and homogeneous materials [9]. Among them, citric acid ($C_6H_8O_7$, CA) has attracted

* Corresponding author at: Facultad de Ingeniería-Departamento de Ingeniería mecánica y mecatrónica, Universidad Nacional de Colombia-sede Bogotá, Colombia.
E-mail addresses: ljcardenasf@unal.edu.co, leydi.cardenas@profesores.uamerica.edu.co (L.J. Cardenas Flechas).

https://doi.org/10.1016/j.mtcomm.2023.106406
Received 15 January 2023; Received in revised form 24 May 2023; Accepted 7 June 2023
Available online 8 June 2023

considerable interest due to its low cost, homogeneity of reaction, applicability in inorganic materials [10], and that it can also serve as a reducing agent [11]. This agent has shown effective results, such as good electrochemical properties [10] and applications in environmental treatment [12]. For example, porous Co_3O_4 structures have been developed [13], and a mesoporous Co_3O_4/TiO_2 structure with a large surface area enables the functional removal of antibiotics in wastewater [14]. In this respect, CTAB fuels and citric acid have been used for the synthesis of Fe_3O_4, $LiMn_{1,5}Ni_{0,5}O_4$ and $Ni_xCo_{3-x}O_4$ [15–17].

Moreover, Co_3O_4-Bi_2O_3 nanocomposites achieved 92% catalytic performance of rhodamine B [18], enhanced surface oxygen adsorption, narrow band gap value, and high lattice distortion: critical aspects of photocatalytic degradation [19]. Synthesized through the aforementioned processes, spinels play a crucial role in various contexts due to the ordered structures formed by the combination of technologies required for their synthesis. For example, FeV_2O_4 and ZTO are used to improve catalytic activity [20,21], $CuFe_2O_4$ to obtain high infrared emissions at low temperatures [22], and stoichiometric $CdGa_2O_4$ spheres for gas detection [23]. Regarding the cobalt-based spinels, significant progress has been made in improving the dielectric properties of Mn-Co_3O_4 [24], for example, in advanced photocatalytic performances, thanks to the advancement of CuO/Co_3O_4 heterostructures [25], and in inverse spinels used as active electrocatalysts in the oxygen evolution reaction with $MnCo_2O_4$ [26]. The development of new photocatalysts has revolutionized the field of environmental remediation, enabling the efficient removal of a wide range of organic pollutants from wastewater and air [27]. Furthermore, NiO/TiO_2 nanoparticles were synthesized and used for the photodegradation of brilliant green (BG), resulting in the formation of intermediate products such as phenol and H_2 [28]. The photocatalyst showed higher efficiency after the addition of NiO due to the p-n heterojunction formation [29].

Recently, rGO has been increasingly used in dye adsorption applications. rGO should have a large surface area and high porosity to enhance this capability. Thus, several studies have reported the use of rGO use in the removal of dye contaminants by photocatalysis, particularly the harmful dye MB from wastewater. And although it has demonstrated excellent adsorption capacity of MB, there is no information on the optimization of its photoactivity. Since rGO behaves as an adsorbent, in addition to its economic and environmental benefits, there is great potential to use it as a photocatalyst [30]. Moreover, reduced graphene oxide added with nickel can achieve a synergistic effect, improving the performance and conductivity in the $Co_{3-x}Ni_xO_4$ composite. Currently, the use of products such as synthetic dyes (methylene blue, eriochrome black, methyl orange) causes environmental problems due to their ultimate deposition in water sources. The rGO-Co_3O_4 nanocomposite exhibits a synergistic effect that makes it suitable for various applications, including catalytic transformation and environmental remediation. It has been proven efficient in reducing 4-nitrophenol and has high adsorption capacity for Cr(VI) and organic dyes. Additionally, it can be easily separated from liquid phase due to its magnetic properties [31]. The Co_3O_4/rGO nanocomposite with oxygen vacancy defects also shows potential for sustainable solar energy conversion, particularly for the photothermal degradation of methanol due to the thermal auxiliary effect of rGO and the oxygen vacancy defects on the surface of Co_3O_4 [32].

This research presents the synthesis of Co_3O_4 doped with various nickel (Ni) percentages using two routes.The first used CA and the second CTAB, among other precursors, in order to establish the effect of both agents in the synthesis of cobalt spinel via the sol-gel technique, selecting the best condition to practice additional doping with reduced graphene oxide (rGO) and evaluating its photocatalytic effect on methylene blue (MB). The $Co_{3-x}Ni_xO_4$ + rGO composite has been studied in other applications but, to our knowledge, not as a photocatalyst for MB.

2. Materials and methods

2.1. Synthesis routes

Route 1: the synthesis of Co_3O_4 and $Co_{3-x}Ni_xO_4$ used as precursors cobalt nitrate hexahydrate ($Co(NO_3)_2{\cdot}6\ H_2O$, Acros) with citric acid monohydrate ($C_6H_8O_7$, Scharlau) in distilled water as solvent. The mixture was stirred for 4 h at 50 °C, and then nickel nitrate hexahydrate ($Ni(NO_3)_2{\cdot}6\ H_2O$, Acros) was added at 1%, 4%, 10%, and 16%. The obtained samples were dried for 10 h in an oven for dehydration. The dried product was subjected to a sintering heat treatment in a muffle furnace at 400 °C, 600 °C, and 800 °C for 3 h.

Route 2: the Co_3O_4 and $Co_{3-x}Ni_xO_4$ were synthesized using as precursors $Co(NO_3)_2.6\ H_2O$, cetyltrimethylammonium bromide ($C_{19}H_{42}BrN$ (CTAB), PanReac), urea (CH_4N_2O, PanReac), and distilled water as solvent. The solution was homogenized by magnetic stirring for 2 h at 60 °C, followed by the addition of $Ni(NO_3)_2.6\ H_2O$ at 1%, 4%, 10%, and 16%. To dehydrate the formed gel, the product was dried for 4 h at 80 °C. The dried derivative was subjected to sintering heat treatment in a muffle furnace at 400 °C, 600 °C, and 800 °C for 3 h. The variation of the molar concentration for the synthesis of Ni-doped Co_3O_4 is observed in Table 1.

The hydrothermal technique synthesized the $Co_{3-x}Ni_xO_4$ + rGO using $CoC_4H_6O_4.4\ H_2O$ hexahydrate cobalt acetate and $NiSO_4.6\ H_2O$ hexahydrate nickel sulfate, CH_4N_2O urea, rGO, and distilled water as precursors. Stirring started at 350 rpm and 100 °C for 3 h, grinding the reduced graphene oxide to ensure compound dispersion. The solution was placed in a hermetically sealed autoclave and heated at 160 °C for 16 h. In the sample preparation for both the sol-gel method and the hydrothermal method with the addition of reduced graphene oxide (rGO), an amount of 0.056 g was added with a stirred mixture for 4 h at 50 °C. The solid powder of reduced graphene oxide rGO was purchased and imported from Virginia, USA, from the supplier Geographene. The description indicates that rGO was prepared by chemical reduction of single-layer graphene oxide (GO) sheets. With specific surface area (BET) measurements on the different samples, the best ones were selected, attending to the synthesis route, nickel addition, and sintering temperature.

2.2. Photocatalytic degradation parameters

RGO was added to the selected samples to study the degradation of methylene blue (MB). The photocatalytic degradation of the MB pollutant was carried out taking 20 mg of samples of $Co_{3-x}Ni_xO_4$ + rGO to 50 mL of 10 ppm methylene blue solution in a photocatalytic reaction system equipped with a visible UV light lamp —G6 Wellness germicidal UV with a power of 25 W in the reaction cell. The value of the pH= 6. All experiments were run at room temperature, and samples with residues were removed with a syringe-driven filter unit. For surface area, the best results were observed in R_1 for 1% and 4% Ni at a sintering temperature of 400 °C. For photocatalytic tests, the different R_1 samples did not include rGO. However, a relevant response was obtained at room temperature in the degradation of MB for 4% Ni.

The concentration of methylene blue in the solutions was analyzed in a UV-Visible P Selecta V1100 D spectrophotometer, measuring at a wavelength of 664.5 nm. For the surface, the test started stirring for 15

Table 1
Variation of molar concentration $Co_{3-x}Ni_xO_4$.

Variation of molar concentration	Molar concentration of Ni (mol)	Molar concentration of Co (mol)
$Co_{3-x}Ni_xO_4$ – Ni 1% wt.	0.03	2.97
$Co_{3-x}Ni_xO_4$ – Ni 4% wt.	0.12	2.88
$Co_{3-x}Ni_xO_4$ – Ni 10% wt.	2.72	0.28
$Co_{3-x}Ni_xO_4$ – Ni 16% wt.	2.52	0.48

min 20 mg of the $Co_{3-x}Ni_xO_4$ and $Co_{3-x}Ni_xO_4$ + rGO photocatalyst obtained by sol-gel and prepared in an aqueous solution of methylene blue. At 15 min intervals, samples were taken from the reactor to evaluate the efficiency of the photocatalyst. Finally, the indicated spectrophotometer analyzed each sample absorption.

2.3. Characterization

Specific surface area (BET) and porosity were determined using Micromeritics Tristar 3000 equipment, nitrogen adsorption at liquid N_2 temperature and carbon black batch: 180049/180052 (21.3 $m^2 \cdot g^{-1}$ ± 0.75) were used as reference material. The degassing process was carried out between 22 and 24 °C for four hours. The pore diameter of the samples was calculated from the Barrett-Joyner-Halenda (BJH) desorption branch.

Crystallinity was determined through X-ray diffraction (XRD) and measurements were performed on the PANalytical X′Pert PRO MPD Bragg-Brentano powder diffractometer with Cukα radiation (λ = 1.5418 Å), an operating power of 45 kV– 40 mA, and a secondary graphite flat crystal monochromator with X′Celerator Detector and 2.122º active length. Diffraction patterns were measured over a 2θ range between 10° and 90°. Analyzes were performed using X′pert High Score Plus software.

Thermogravimetric (TG) analyzes were performed on TA Instruments Q-600 SD from 30 °C to 1100 °C at a heating rate of 10 °C·min^{-1}, sensitivity of the balance: 0.1 μg, calorimetric accuracy: ± 2%, and using a platinum-rhodium thermocouple. The morphology of the samples was characterized by field-emission scanning electron microscopy (FESEM, Nijmegen, The Netherlands) (FESEM-JEDL J-7100). Raman analysis was performed using a Jobin-Yvon LabRam HR800 dispersion spectrometer, laser line 532 nm. Fourier transform infrared spectroscopy (FT-IR) was performed on a Perkin-Elmer Spectrum Two spectrometer equipped with a standard optical system with KBr windows for data collection in the spectral range of 8300–350 cm^{-1} with an optimum resolution of 0.5 cm^{-1} and a standard, high performance, room temperature $LiTaO_3$ MIR detector with an SNR of 9300:1.

3. Results and discussion

The aim of the analysis was to thoroughly characterize the samples and provide information on their suitability for the catalytic degradation of methylene blue. By investigating the specific surface area, phase, morphology, optical, vibrational and electrical properties, the aim was to identify the most efficient catalysts and understand the underlying mechanism of the degradation process. These findings will help to optimize the conditions for methylene blue degradation and potentially lead to more effective and sustainable catalytic processes.

3.1. Specific surface area study

Table 2 shows the results of R_1-CA and R_2-CTAB for the analysis of the specific surface area of the samples. As the final calcination temperature increases, the specific surface area decreases. According to Liu et al. [33], the sample calcinated at lower temperatures obtained the highest surface area, indicating that the BET-specific surface areas for Co_3O_4 vary downwards with different calcination temperatures. In terms of surface area, the Ni and rGO effect is best observed at 400 °C since, at higher temperatures, the pores are destroyed as the oxides sinter.

The samples at 600 °C for 10% and 16% Ni for the R_1 have a larger pore volume. However, they do not have a large specific surface area, but this volume should not be the deciding factor. If it is the main issue, the photocatalytic efficiency of the samples at 10% and 16% Ni should be higher in the photocatalysis experiment. Therefore, it can be stated that the pore size, distribution, and number have a decisive impact on the surface area for MB degradation. According to the literature, the ideal photocatalyst for MB should have a mesoporous structure with a good adsorption performance and a large specific surface area [34].

At 800 °C, the specific surface area values remain in an average range of 1.8 $m^2 \cdot g^{-1}$ for R_1-CA and 1.6 $m^2 \cdot g^{-1}$ for R_2-CTAB, the lowest values obtained for the rest of the sample, as the oxides have been sintered and destroy the pores. At 600 °C, the specific surface area values of R_2 show a considerable (higher) variation for R_1-CA, with a difference of 3 $m^2 \cdot g^{-1}$ for 1% and 4% Ni doping. At 400 °C, the 4% Ni-doped samples have the highest values with 21.2 $m^2 \cdot g^{-1}$ and 19.1 $m^2 \cdot g^{-1}$, and pore sizes of 190.42 Å and 554.41 Å for R_1-CA and R_2-CTAB, respectively. The purpose of this section is to investigate the specific surface area of the samples, R_1-CA and R_2-CTAB, and to understand how it is affected by different calcination temperatures. The results are compared with previous studies in the literature to validate the findings and to show the effect of pore size, distribution and number on the specific surface area and photocatalytic efficiency for methylene blue degradation. The aim is to provide insight into the best conditions for the synthesis of photocatalysts with optimal properties for the degradation of methylene blue.

From these data, it can be hinted that the CA used in R_1 generates nanostructures with higher specific surface area values compared to CTAB employed in R_2 for 4% Ni doping at 400 °C. Pudykydy et al. [33, 35] reported that the preparation of cobalt spinel with citric acid obtained the highest specific surface area value (29 $m^2 \cdot g^{-1}$) compared to other modifiers.

With this information, it can be inferred that the 1% and 4% Ni at a temperature of 400 °C present the best surface area values in both synthetic routes: the highest were 18.15 $m^2 \cdot g^{-1}$ and 21.18 $m^2 \cdot g^{-1}$ for 1% and 4% Ni in R_1, respectively, and 18.1 and 19.13 $m^2 \cdot g^{-1}$ for 1% and 4% in R_2. This information is relevant because the surface area

Table 2
Specific surface area and pore analysis.

		R_1-CA route			R_2-CTAB route		
Temp. (°C)	% Ni	Surface area ($m^2 \cdot g^{-1}$)	Average pore size (Å)	Pore volume (cm^3 g^{-1})	Surface area ($m^2 \cdot g^{-1}$)	Average pore size (Å)	Pore volume (cm^3 g^{-1})
400	1.0	18.158	195	0.08	18.967	281.97	0.13
	4.0	21.184	190.0	0.10	19.132	554.41	0.26
600	Co_3O_4 0.0	3.817	552.70	0.05	6.509	329.12	0.05
	1.0	3.948	538.97	0.05	7.302	310.10	0.05
	4.0	4.343	491.41	0.05	7.341		
	10.0	3.294			6.974		
	16.0	4.194			6.803	309.69	0.05
800	Co_3O_4 0.0	1.499	296.51	0.01	1.276	227.77	0.07
	1.0	1.826	423.11	0.19	1.438	105.76	0.05
	4.0	2.143	162.01	0.08	1.632	199.13	0.08
	10.0	1.408			1.835		
	16.0	1.761			1.655		
400	1 +rGO	31.372	530	0.12			
	4 +rGO	84.743	630	0.18			

properties play an important role, especially for photocatalytic applications.

Therefore, the following lines focus on these samples, analyzing their characteristics and their synthesis through the two routes (R_1-CA and R_2-CTAB). For the sample with the addition of rGO at 1% and 4% Ni, a much larger overcharge area is observed compared to the other samples with values of 31.36 $m^2 \cdot g^{-1}$ and 84.7 $m^2 \cdot g^{-1}$, respectively. However, the combination of Co_3O_4 and rGO nanostructured material has been studied for high energy, power density, and long lifetime supercapacitors. The authors found specific areas of ~87.8 $m^2 \cdot g^{-1}$ with a higher specific capacitance [36]. For this reason, the results obtained for the sample with 4% Ni and rGO addition are comparable to those found in the literature. The presence of rGO increases the specific surface area of the material, and better performance in the photocatalytic activity of the MB is expected. When observing the pore size in the samples, there are significant differences, however, the surface area is not only defined by the diameter but also by the number of pores.

The surface area is a decisive study parameter in the photocatalytic efficiency of MB since a large surface area means more active sites for catalysis. Decrease in surface area, partial loss of structural order, and growth of crystallites due to sintering at high temperatures affect the photocatalytic activity of the material. In this case, in the 1% and 4% Ni in Co_3O_4 + rGO samples, the BET-specific surface area increased considerably, as did the pore volume. Therefore, as expected, it was improved by introducing rGO into the nanocomposite, giving higher values for 4% Ni (surface area 84.7 $m^2 \cdot g^{-1}$ and pore volume 0.18 $cm^3 \cdot g^{-1}$). As Table 2 illustrates, the pore volume for R_1 at 400 °C and 4% Ni, with and without rGO addition, was always greater than 1% Ni, as was the specific surface area. The larger the specific surface area, the greater the number of active sites for photodegradation of the MB.

According to Fan et al. [37] the in-situ deposition of electrosprayed Co_3O_4 nanoparticles on a substrate resulted in good acetone sensitivity, selectivity, and stability. The sensor showed excellent linearity over the acetone concentration range of 1–50 ppm at an optimum working temperature of 200 ºC, and sub-ppm acetone could be detected. Moreover, the synthesis of Co_3O_4 nanoparticles was found to be highly dependent on the type of solvent used in the synthesis, which suggests that the solvent-dependent synthesis approach can be an effective strategy for tuning the morphology and properties of cobalt tetraoxide nanoparticles for gas sensing applications [38]. In this work Co_3O_4/rGO nanocomposites with 1% and 4% Ni doping concentrations exhibited high sensitivity to acetone at room temperature. The sensitivity to acetone was higher for the Co_3O_4/rGO nanocomposite with 4% Ni doping concentration, which had a higher specific surface area. The high sensitivity to acetone could be due to the changes in the surface chemistry of the Co_3O_4/rGO nanocomposites caused by the presence of rGO.

3.2. Evaluation of phase composition

In order to determine the crystalline structure of the synthesized samples based on the conditions applied, X-ray diffraction analysis was carried out. The XRD patterns of the samples obtained undoped and doped with 1% and 4% Ni are observed in Fig. 1a-f. The peaks correspond to the unique spinel structure of cobalt oxide Co_3O_4 with a preferred orientation at (311) and no secondary phases [39]. The identified coincident planes are associated with standard XRD data (ICSD-36256) [40] and space group *Fd-3 m* [41].

In the samples obtained by R_1-CA, a higher intensity in the diffraction peaks is observed than in those obtained by R_2-CTAB. Citric acid provides the combustion to calcinate the cobalt tetraoxide, forming the oxide phase at low calcination temperatures. In this case, 400 °C, through the reaction between metal ions [42]. The crystallite size of the obtained samples was calculated using the Scherrer equation for the highest intensity peaks (311), (511) and (440).

The crystallite size analyses indicate that for R_1-CA, the average value is 23.05 nm for the (311) plane, while for R_2-CTAB, it is 15.42 nm,

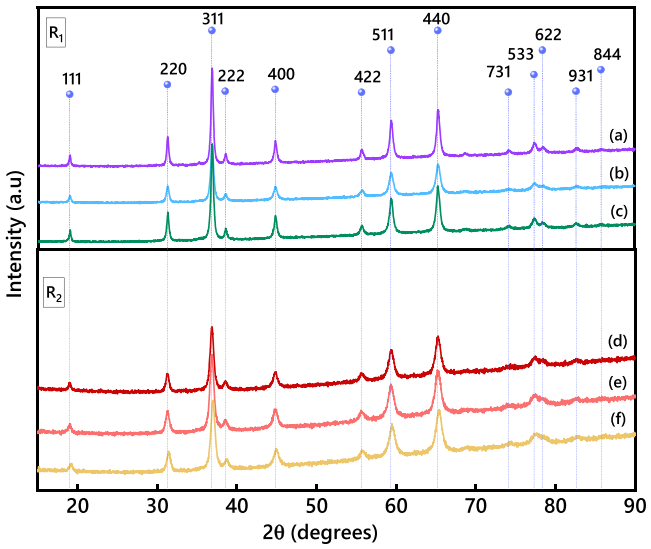

Fig. 1. XRD diffraction patterns: R_1 with (a) Co_3O_4, (b) 1% Ni and (c) 4% Ni, and R_2 with (d) Co_3O_4, (e) 1% Ni and (f) 4% Ni.

as shown in Table 3 where a decrease in size is observed as nickel doping increases, reaching 14.18 nm in 4% Ni. These results can be associated with the effect of CTAB in the synthesis for R_2 since the particle size is related to the reduction of nanoparticle growth by disintegrating the agglomerate. Consequently, when nano-powders are obtained, low agglomeration and particle size distribution can be achieved through the sol-gel method by adding a cationic surfactant, such as cetyltrimethylammonium bromide CTAB [43], which changes the thermal behavior of the products [1].

Fig. 2 shows the XRD diffraction patterns of Co_3O_4 at 4% Ni + rGO. Due to the reduced graphene oxide, the crystallographic peak intensities decrease while maintaining the spinel phase of Co_3O_4. X-rays showed characteristic peaks at $2\theta = 31.3°$, 36.8°, 44.8°, 59.4°, and 65.2°, which were assigned to (220), (311), (400), (511), and (440) of the spinel cubic planes of Co_3O_4, respectively. The results indicate that crystalline Co_3O_4 has been formed after the thermal calcination process.

Only diffraction peaks of $Co_{3-x}Ni_xO_4$ are detected in the $Co_{3-x}Ni_xO_4$ + rGO composite, suggesting that the synthesized nanoparticles completely cover the rGO, agreeing with the Raman analysis. Moreover, compared with pure Co_3O_4, all the characteristic peaks of the $Co_{3-x}Ni_xO_4$ + rGO composite are broader and of lower intensity. The crystallite size of the $Co_{3-x}Ni_xO_4$ + rGO nanocomposite is estimated to be ~20 nm, as shown in Table 4, and agrees with the TEM image (Fig. 3a). These nanometer-scale particles are beneficial because they provide more accessible interfaces to favor ion diffusion.

3.3. Morphological characterization

In order to visualize the shape, size and texture of the $Co_{3-x}Ni_xO_4$ samples, SEM analysis was performed. Fig. 3a-d presents the SEM micrographs obtained by R_1-CA and Fig. 3e-f by R_2-CTAB. The analyses indicate a larger particle size in the samples where R_1-CA was used compared to the obtained by R_2-CTAB. According to Ahmadi et al. [44], the addition of CTAB generates a particle size distribution of lower value and greater uniformity, which prevents agglomeration and overgrowth. In turn, the addition of CTAB could have a relevant effect on the composite morphology, especially inducing the formation of nanoplates due to the growth of the crystalline face of the Co_3O_4 crystals by the absorption of the surfactant in the system [45].

The sample microstructure can change due to a complexing agent, such as CA, which acts in the reaction and influences the particle size [46]. In SEM micrographs, particles with irregular morphology,

Table 3
Cristallite size of the Co_3O_4 samples obtained by routes R_1 and R_2.

Sample	FWHM (°)						Cristallite size (nm)		
	Pos. (2Θ)	(311)	Pos. (2Θ)	(511)	Pos. (2Θ)	(440)	(311)	(511)	(440)
R_1 – Co_3O_4	36,86	0324	59,36	0,42	65,24	0,40	25,83	21,81	23,57
R_1 – 1% Ni	36,85	0,43	59,30	0,61	65,23	0,62	19,55	14,91	15,30
R_1 – 4% Ni	36,86	0,35	59,35	0,48	65,23	0,48	23,78	19,12	19,60
R_2 – Co_3O_4	36,85	0,53	59,33	0,75	65,22	0,75	15,68	12,18	12,57
R_2 – 1% Ni	36,79	0,51	59,32	0,81	65,21	0,81	16,40	11,28	11,63
R_2 – 4% Ni	36,87	0,59	59,27	0,88	65,16	0851	14,18	10,38	11,07

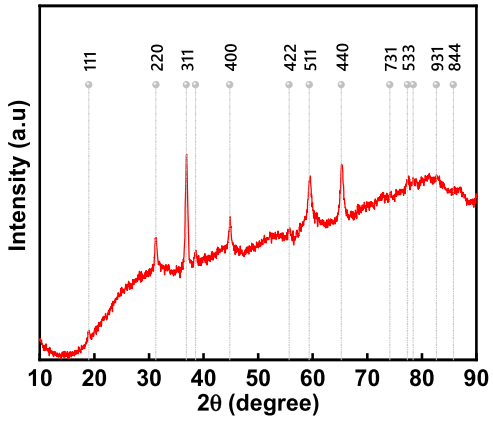

Fig. 2. XRD diffraction patterns of Co_3O_4 at 4% Ni + rGO.

hemispherical shape, and larger agglomerates for R_1-CA are observed. Du et al. [47] reported that Ni doping did not cause significant changes in morphology. However, in the present study, morphological and particle size modifications were observed even without Ni addition. This suggests that other factors, such as the synthesis method or the precursor materials, may have played a role in the observed modifications.

Fig. 3a shows the material for R_1-CA without Ni addition at 400 °C. This micrograph reveals particle aggregation without forming distinct particles. Fig. 3b shows 1% Ni for R_1-CA. Fig. 3b shows 1% Ni for R_1-CA with non-uniformly shaped particles. Fig. 3c presents the SEM for 4% R_1-CA, and the addition of Ni decreases the particle size and globular morphology, increasing the surface area, as observed in Table 2. Fig. 3d reflects the sample at 4% Ni + rGO for R_1-CA. In this case, the particle size seems to decrease with the rGO addition. Still, the morphology and shape of the particles are irregular. Fig. 3e-f represents the samples for R_2-CTAB at 1% and 4% Ni, respectively, where the particles are less agglomerated, and their size decreases with Ni addition.

The morphologies of $Co_{3-x}Ni_xO_4$ + rGO nanocomposites (1% and 4% Ni) were analyzed by TEM (Fig. 4a-b). TEM micrograph revealed the spheroidal morphology of the nanoparticles (NPs). As it indicates, these are less than 20 nm and much smaller for 4% Ni + rGO than for 4% Ni + rGO (Fig. 4a). The $Co_{3-x}Ni_xO_4$ + rGO composite in Fig. 4b is observed with a unique morphology, different from that of 4% without adding rGO. rGO favored the consistent growth of $Co_{3-x}Ni_xO_4$ nanoparticles on it, preventing the re-stacking of graphene nanosheets and providing a larger surface area [48].

According to the literature, carbon materials combination with Co_3O_4 is an effective way to improve electrochemical performance, especially the power density, energy density, cycle stability, and electrode rate performance. Co_3O_4 nanoparticles, with an average size of ~15 nm, adhere to the surface of rGO films and serve not only as spacers to suppress the stacking of rGO films effectively but also as a stabilizer to prevent the decomposition of the $Co_{3-x}Ni_xO_4$ + rGO structure during heat treatment [48]. It can be deduced that the rGO is being coated by the $Co_{3-x}Ni_xO_4$ nanoparticles since an arrangement of the particles in a chrysanthemum-like cluster is observed.

3.4. Diffuse reflectance analysis and band gap determination in $Co_{3-x}Ni_xO_4$ nanostructures

In order to gain a deeper understanding of the molecular level transitions in the synthesized material, a diffuse reflectance ultraviolet-visible spectroscopic characterization was carried out. Fig. 5 shows the diffuse reflectance spectra obtained for Co_3O_4 samples without nickel doping and with doping at 1% and 4% Ni by R_1 and R_2, respectively and Tauc plot optical band gap. On the one hand, a variation in the bandgap (E_g) of the samples obtained by R_1 is observed, with values of 1.81 eV for the undoped sample and 1.72 eV for the 4% nickel-doped sample. On the other hand, E_g values remain constant between 1.71 and 1.72 eV for R_2.

These results can be associated with previous ones [49], where a decrease in the band gap is observed for nickel doping of Co_3O_4, going from E_g = 5.57–3.71 eV. According to Agilandeswari et al. [50], the positive hole exchange between Co^{3+} and Co^{2+} transfers O^{2-} between the vacant oxygen side and the occupied side due to the presence of cobalt ions in two different oxidation states. This smaller energy gap between the 4% Ni of R_1-CA and the surface is substantial for photocatalytic activity.

3.5. Effect of doping on vibrational modes and absorption bands by Raman and FTIR spectroscopy for $Co_{3-x}Ni_xO_4$ + rGO samples

Fourier transform infrared (FT-IR) and Raman spectroscopy characterizations were conducted to analyze the molecular vibrations of the synthesized samples. Fig. 6a-f points to the Raman spectra of the samples synthesized by R_1-CA and R_2-CTAB. The five active modes corresponding to the spinel structure of cobalt oxide are indicated, with peaks at 190, 471, 513, 609, and 677 cm^{-1}. In both routes, shifts in the vibrational modes are observed, becoming more visible with higher nickel doping. There is a considerable difference in the intensity of the peaks, whose visibility is higher in the $A_{1\ g}$ mode. Also, this can be attributed to the insertion of Ni into the Co_3O_4 lattice with shifts and propagation of the peaks related to electronic disorder in the octahedral sites of the cobalt spinel [51].

Table 5 shows the mode position values for R_1 and R_2, where the E_g

Table 4
The cristallite size of the $Co_{3-x}Ni_xO_4$ + rGO sample, obtained by R_1.

Sample	FWHM (°)						Cristallite size (nm)		
	Pos. (2Θ)	(311)	Pos. (2Θ)	(511)	Pos. (2Θ)	(440)	(311)	(511)	(440)
R_1- 4% + rGO	36.84	0.32	59.35	0.48	65.23	0.58	27.3	19.9	16.9

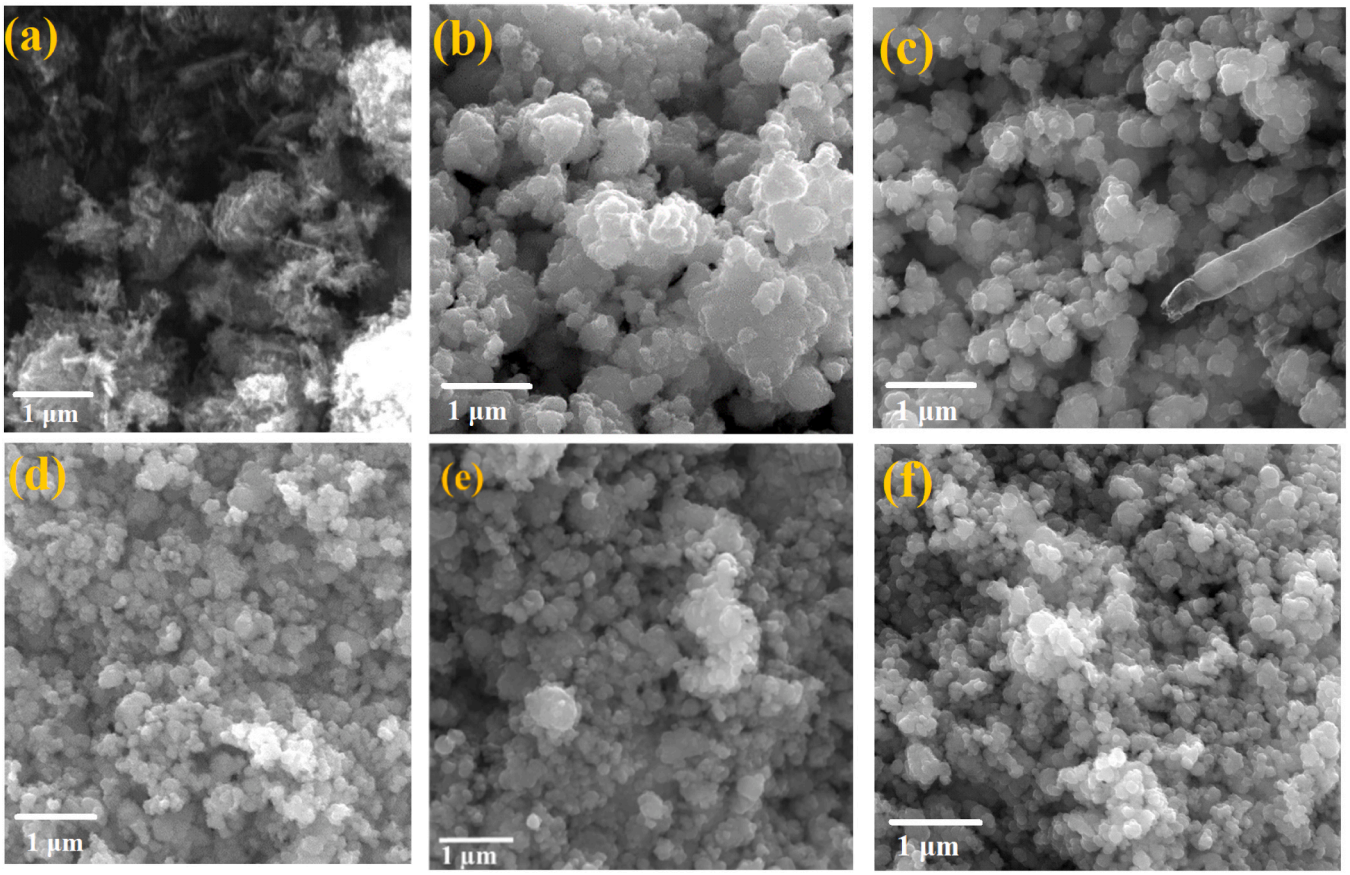

Fig. 3. SEM micrographs at 400 °C. R_1: (a) Co_3O_4, (b) Co_3O_4, 1% Ni, (c) Co_3O_4, 4% Ni, (d) Co_3O_4, 4% Ni + rGO and R_2: (e) Co_3O_4,1% Ni, (f) Co_3O_4, 4% Ni.

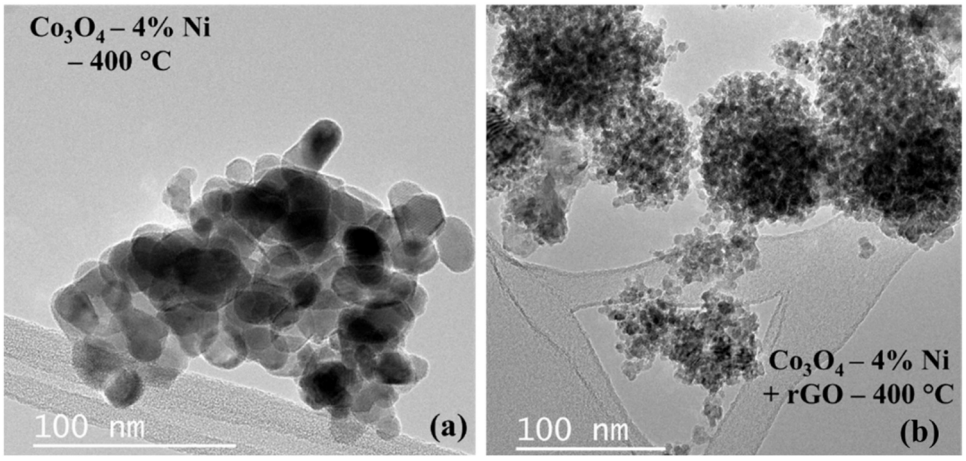

Fig. 4. R_1-CA at 400 °C. (a) TEM image of Co_3O_4 of 4% Ni, (b) TEM of Co_3O_4 of 4% Ni + rGO.

mode presents a variation of 5.47 cm^{-1} (R_1-CA) and 5.04 cm^{-1} (R_2-CTAB). It is also true for the $F_{2\,g}$, $F_{2\,g(1)}$, $F_{2\,g(2)}$, and A_{g1} modes. For a Ni concentration of 4%, the peaks decrease in intensity and shift towards lower frequencies, indicating that the spinel structure changes, as seen in Figs. 6c and 6f. Observing the vibrational modes of the samples, as the nickel concentration increases, a shift for low frequencies and a mid-height length in the Raman peaks due to the distortion of the lattice studied in both routes is appreciated.

As it is noticed, for rGO (Fig. 7a), there are two broad peaks centered at 1343 and 1596 cm^{-1}, corresponding to the D and G bands, respectively. Altogether, the D band is related to the defective/disordered domain, and the G band is assigned to the $E_{2\,g}$ phonon. In the $Co_{3-x}Ni_xO_4$ and $Co_{3-x}Ni_xO_4$ + rGO nanocomposites, the characteristic peaks originating from the reduced graphene oxide disappear, and new distinctive peaks of Co_3O_4 appear, located around 187, 479, 512, 671, 846 cm^{-1}, corresponding to the vibrational modes of the Co_3O_4 structure.

The data agree with those reported for the standard microcrystalline Co_3O_4 powder. The disappearance of the characteristic peaks corresponding to reduced graphene oxide (rGO) in the $Co_{3-x}Ni_xO_4$ + rGO nanocomposite can be attributed to the complete coverage of $Co_{3-x}Ni_xO_4$ nanoparticles of rGO, further confirming the formation of

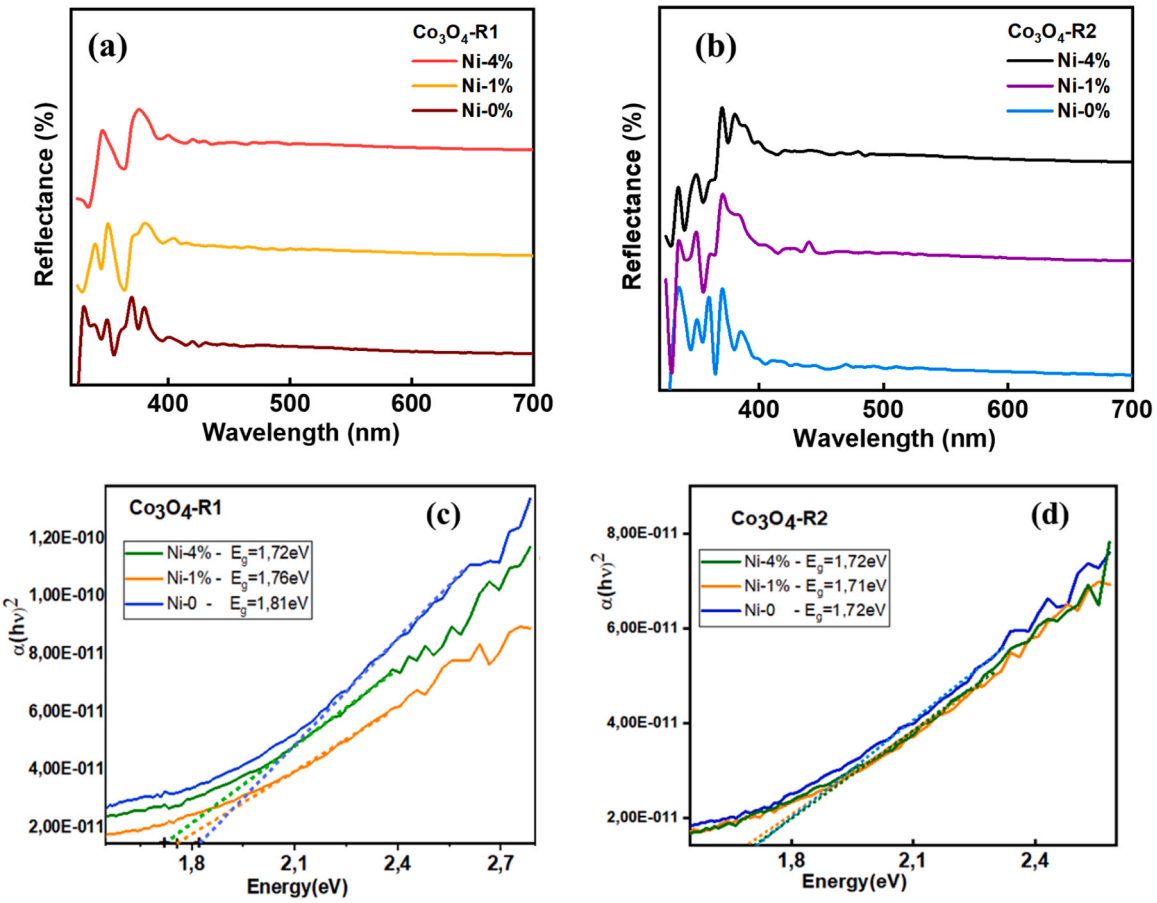

Fig. 5. UV-Vis spectra (a,b) and Tauc plots (c,d) with optical band gap evaluation for Co_3O_4-R_1 and R_2, both without Ni doping and with 1% and 4% Ni doping.

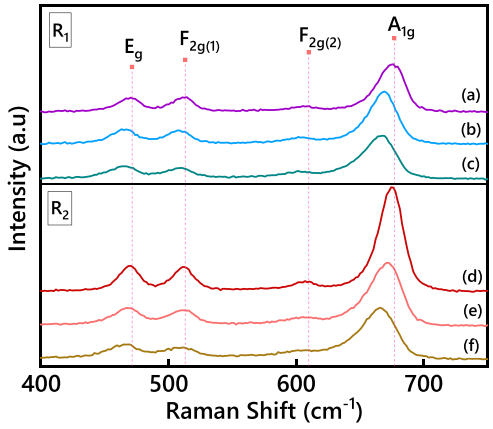

Fig. 6. Raman Spectra for Co_3O_4-R_1 (a) without nickel doping and (b) with 1% and (c) 4% Ni doping, and for Co_3O_4-R_2 (d) without nickel doping and (e) with 1% and (f) 4% Ni doping.

Table 5
Raman Shift displacement.

	Raman Shift (cm^{-1})					
R_1	**Sample**	**$F_{2\,g}$**	**E_g**	**$F_{2\,g(1)}$**	**$F_{2\,g(2)}$**	**A_{g1}**
	(a)	188.28	470.08	512.95	607.43	677.10
	(b)	186.09	465.34	508.39	603.23	668.90
	(c)	185.63	464.61	508.01	602.14	666.34
R_2	(d)	188.82	470.93	513.31	607.25	675.46
	(e)	187.36	468.62	511.49	604.51	672.36
	(f)	184.81	465.89	509.66	-	665.61

TEM measurements, where ordered nanoparticles forming almost a chrysanthemum are observed [52]. With the increase in Ni concentration in the crystal lattice and the addition of rGO, the Raman modes lose intensity and underGO a length in their half-height, indicating disorder in the lattice.

Fig. 8a-c shows the FTIR spectra for the samples obtained by R_1 and Fig. 8d-f for those obtained by R_2. The analyses indicate two absorption bands located at 653 cm^{-1} and 537 cm^{-1} for R_1-CA, and 652 cm^{-1} and 547 cm^{-1} for R_2-CTAB, confirming the formation of Co_3O_4. In addition, a considerable difference of 10 cm^{-1} is evident in the synthesis with CTAB (R_2). The Figure reveals no additional absorption peaks. More spectroscopic bands are neither observed, which points to an optimal decomposition of CA and CTAB used as precursors in the reactions coming from the sol-gel method. In conformity with Chen et al. [53], citric acid inhibits the segregation of metal ions through coordination with metal ions, allowing homogeneity of the precursor.

3.6. Specific surface area and pore volume for $Co_{3-x}Ni_xO_4$ + rGO samples

Considering that factors such as specific surface area, volume, and pore distribution can affect various applications such as photocatalytic degradation, sorptometric analysis was carried out to gain a comprehensive understanding of these characteristics. Fig. 9a-d includes the adsorption-desorption isotherms of the 1% and 4% Ni-doped samples by R_1-CA and R_2-CTAB. As can be seen, both isotherms are of type IV, with H3 hysteresis loop according to IUPAC, mesoporous distributions, and ordered texture, which is characteristic of this type of nanostructures.

The adsorption isotherms show the formation of large hysteresis loops varying between P/P_0 from 0.62 to 0.96 and are attributed to the

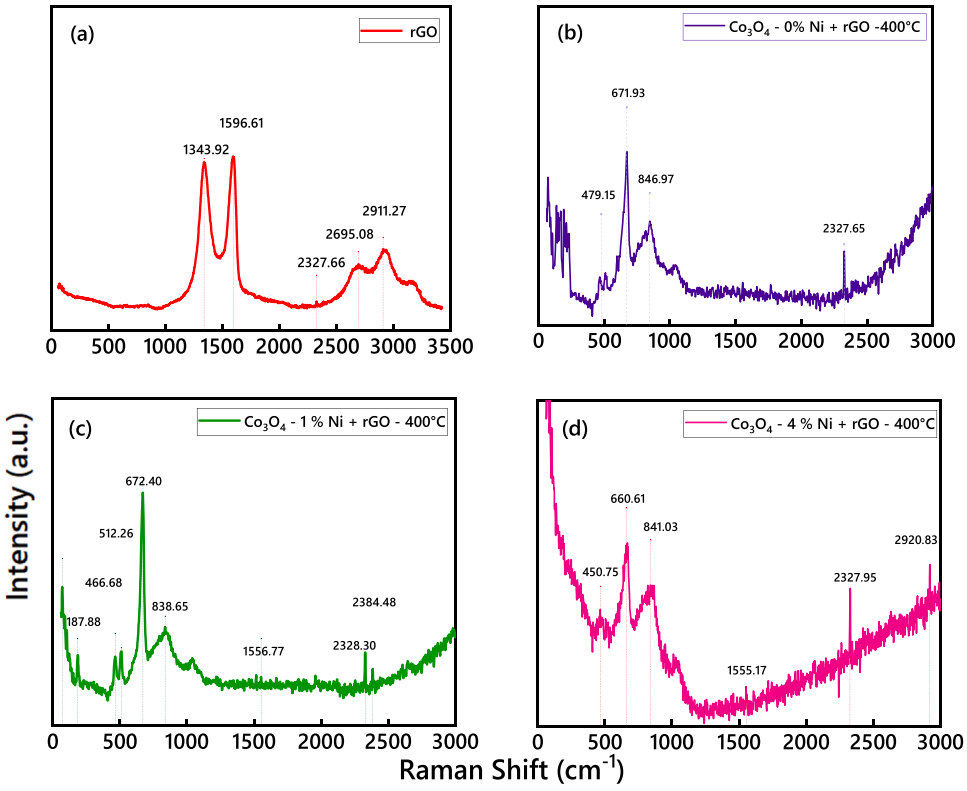

Fig. 7. Raman Spectra (a) rGO, (b) $Co_{3-x}Ni_xO_4$ x = 0% + rGO-R_1 CA, (c) $Co_{3-x}Ni_xO_4$ x = 1% + rGO-R_1 CA, and (d) $Co_{3-x}Ni_xO_4$ x = 4% + rGO-R_1 CA.

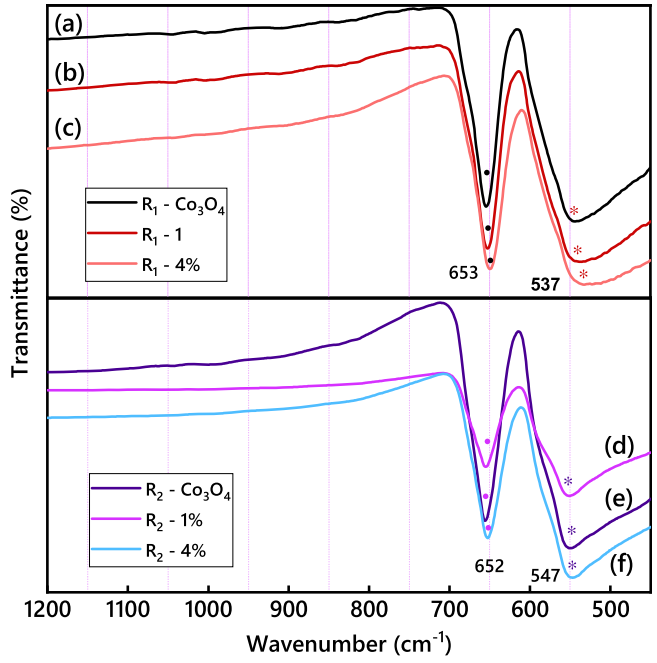

Fig. 8. FTIR spectra for Co_3O_4-R_1 (a) without nickel doping and (b) with 1% and (c) 4% Ni doping, and for Co_3O_4-R_2 (d) without nickel doping and (e) with 1% and (f) 4% Ni doping.

mesoporosity of the particles. These results agree with those presented by Liu et al. [33]. Slight differences in the isotherm shapes of the samples are observed, possibly due to the pore structures formed using different types of reagents to obtain nickel-doped Co_3O_4. Sintering and densification associated with the temperature increase may influence the behavior generated by the curves [54].

Fig. 9e indicates the N_2 adsorption/desorption isotherms for the 4% Ni + rGO sample, which exhibits a typical IV isotherm with a hysteresis loop indicating the presence of mesopores. The specific surface area for this $Co_{3-x}Ni_xO_4$ + rGO sample is calculated to be ~ 84.743 m^2 g^{-1}. Moreover, the existence of rGO effectively increases the specific surface area of the material, playing an important role in MB degradation.

3.7. *Magnetic behavior of $Co_{3-x}Ni_xO_4$ samples x = 0, 1, 4%*

Plotting the magnetization (M) as a function of the magnetic field (H) at a temperature of 300 K, it is observed that the material behaves paramagnetic. However, for the samples obtained by R_1, small changes, more notable for 1% Ni, are visible, as reflected in Fig. 10. In the case of the synthesis by R_2, no changes are noticed with nickel concentration, however, the material displays paramagnetic behavior. According to Takada et al. [55], at 5 K, the magnetization curves showed no hysteresis loops. Furthermore, the magnetic ratio rate improves as the field approaches zero.

The samples have a paramagnetic behavior for the two synthesis routes, possibly related to the magnetization value that increased with the strength of the applied field, giving this result. Also, the use of citric acid for the sol-gel synthesis of the samples influences the morphology and the magnetization values, as does the double exchange interaction through the magnetic nickel dopant ions present as ferrimagnetic impurities in coexistence with the main phase.

According to the analyzes undertaken and descriptions in the literature, the variations that occur in the magnetization with different resistance states can be associated with the concentration of oxygen vacancies and the conversion of the valence states of the cations (Co^{2+}/Co^{3+}). For the cobalt spinel, Co^{3+} ions show no net magnetic moment due to the paired d-electrons, and the corresponding Co^{2+} ions feature magnetic moments from three unpaired d-electrons [56].

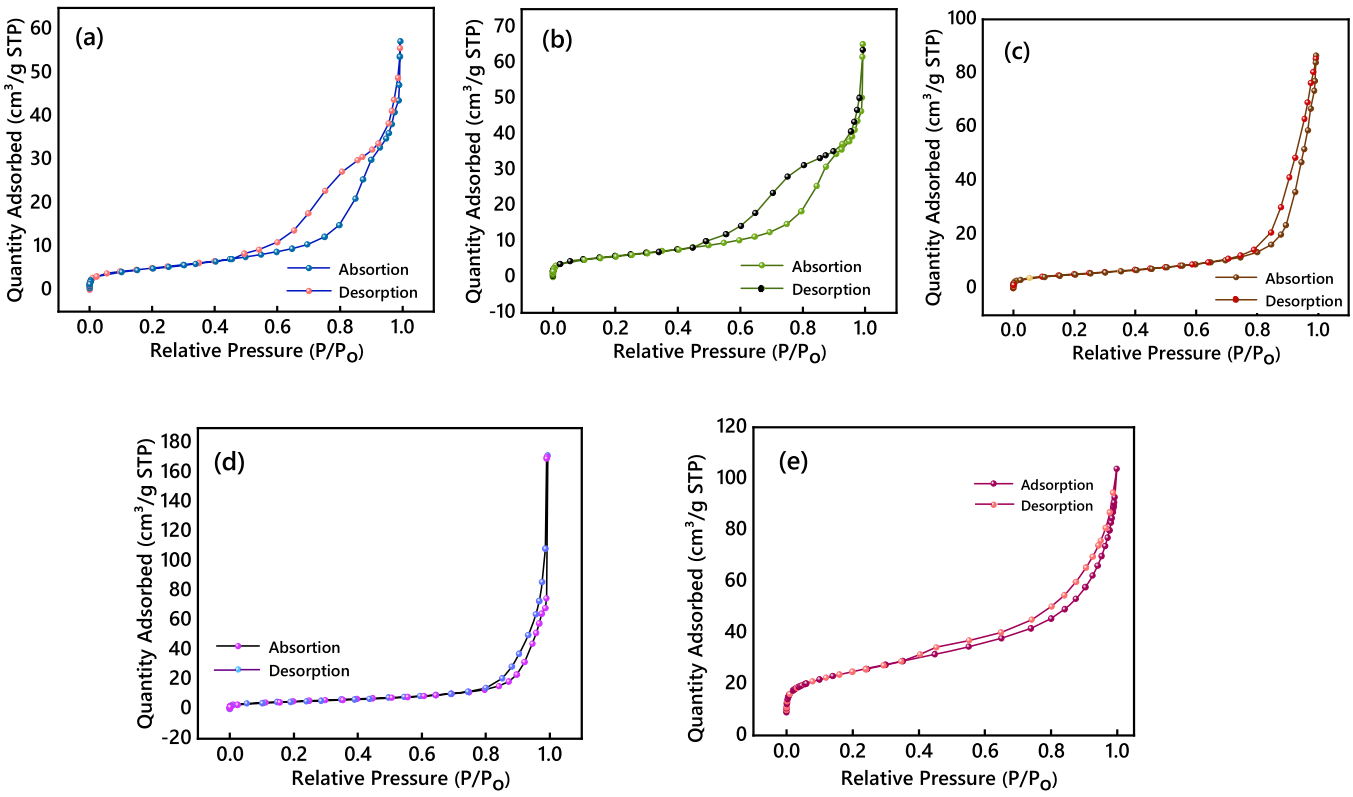

Fig. 9. N_2 Adsorption-Desorption Isotherms at 400 °C for Co_3O_4 with various Ni contents and rGO: (a) R_1 - 1% Ni, (b) R_1 - 4% Ni, (c) R_2 - 1% Ni (d) R_2 - 4% Ni and (e) Co_3O_4 + 4% Ni + rGO.

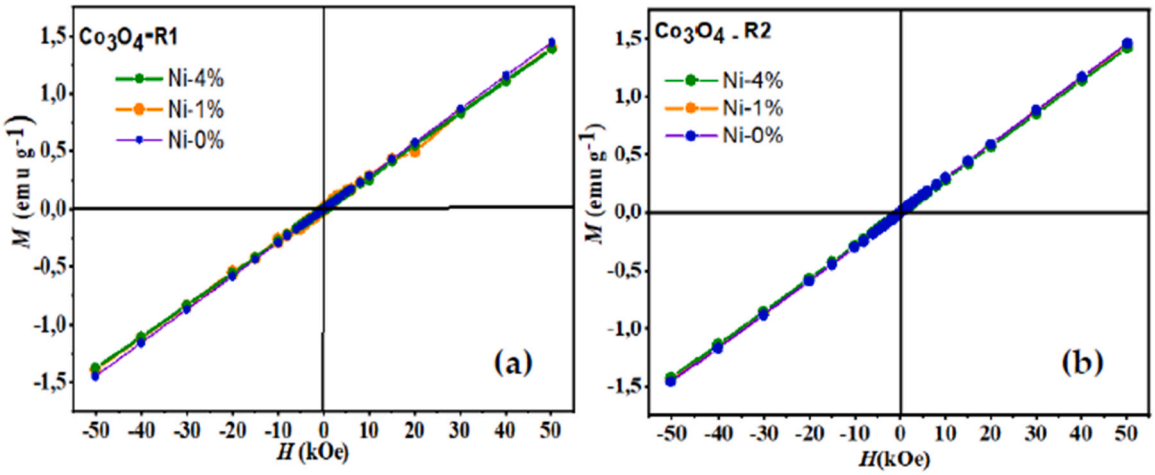

Fig. 10. Magnetization (M) as a function of magnetic field (H) of 0%, 1%, and 4% Ni doped samples synthesized by (a) R_1-CA and (b) R_2-CTAB.

3.8. Photocatalytic degradation of methylene blue

Fig. 11 demonstrates the degradation of methylene blue with $Co_{3-x}Ni_xO_4$ + rGO and without catalyst (NC) under UV light. The results indicate a photocatalytic degradation efficiency evidenced throughout the test. With a catalyst (C), in the first 15 min, the degradation is 21.72%, in 30 min, it is 27.53%, after one hour, 33.62%, and in 2 h, 39.65%. Without catalyst (NC), it starts at 15 min with 1.35% and ends at 120 min with 1.46%. In the case of organic-type dyes, the degradation originates from the electron/hole pairs on the surface, providing a high number of adsorption sites for methylene blue molecules [57].

It is possible to infer that the synergy of cobalt and nickel oxide semiconductor-based compounds and the addition of reduced graphene oxide have a high-performance effect on photocatalytic degradation.

The addition of rGO to the samples improves carrier transport. Besides, the unique porous structure and large surface areas favor the adsorption of molecules in photocatalytic degradation. As seen in Fig. 11, the degradation of MB with 4% Ni Co_3O_4 offers lower degradation compared to the 1% and 4% Ni samples with the addition of rGO and is much better for the 4% Ni sample. These results match those obtained for the specific surface area, resulting in better for this sample. The MB in solution diffuses on the surface of the $Co_{3-x}Ni_xO_4$ + rGO composite particles and adsorbs on the active sites in the adsorption phase. According to the results, the $Co_{3-x}Ni_xO_4$ + rGO samples for 1% and 4% Ni for R_1 CA are mesoporous and favor absorption before oxidation in the photocatalytic process.

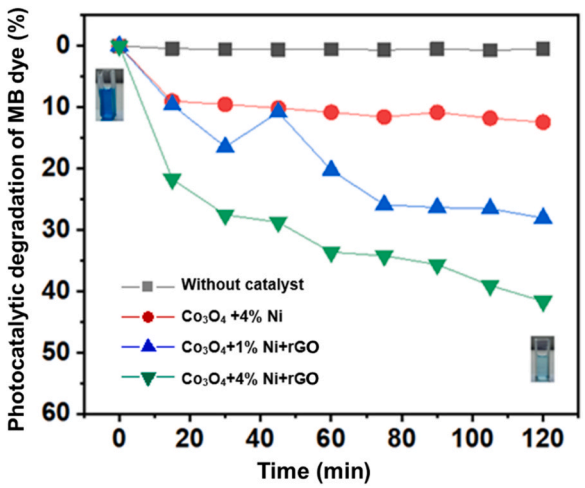

Fig. 11. Absorption of methylene blue with $Co_{3-x}Ni_xO_4$ + rGO samples and in the absence of the nanocomposite (NC) at 120 min.

Therefore, the change in pore size and surface area constitutes a pivotal aspect in the degradation of MB, which is a large molecule and cannot diffuse into smaller pores even if the sample has a large surface area. For this reason, it is also necessary to highlight the influence of pore size on catalytic performance. The $Co_{3-x}Ni_xO_4$ + rGO samples for 1% and 4% Ni for R_1 CA have larger pore volumes and higher photocatalytic degradation efficiency, as shown in Fig. 11 [34].

By analyzing the results obtained through the study of the properties of $Co_{3-x}Ni_xO_4$ and doped with rGO it is possible that the hemispherical and irregular nanomorphology of the nanoparticles obtained in the present investigation, as well as the chrysanthemum-like arrangement revealed in the morphological characterization have given way to the formation of active sites that facilitate the interaction in the photocatalytic degradation of methylene blue. The addition of nickel ions and graphene oxide (rGO) influenced the particle size and morphology.

Several researchers report that the morphology of Co_3O_4 is related to the catalytic performance, more Co^{3+} cations in the (110) planes can provide sufficient sites for ethylene and oxygen adsorption [58] since in metal oxide nanoparticles, some properties strongly depend on the shape and size of the crystallite, as the surface structure as well as electronic and optical properties can change at different levels depending on the nanometer size, crystallographic structure and synthesis method [59].

Moreover, according to Yang et al. [60], the textural and structural properties influence the adsorption-desorption of dyes on the surface of the photocatalyst, which enhances the degradation of dye molecules, and also a minimizes in the hole-electron recombination process [61].

According to the adsorption/desorption isotherms, the photocatalytic activity of the doped samples can be enhanced because the mesopores of the rGO-doped compounds will act as passive channels that facilitate the transport of methylene blue. The $Co_{3-x}Ni_xO_4$ + rGO samples for 1% and 4% Ni for R_1 CA have larger pore volumes and higher photocatalytic degradation efficiency, which is observed in the degradation of MB. The results are consistent with the specific surface area of the material, resulting in better performance for the 4% Ni sample, corroborating that an easy transport of reactive molecules to the active sites during the catalytic reaction can be favored by a high specific surface area [62], suggesting that the addition of rGO enhances carrier transport and the large surface areas of the material favor the adsorption of molecules in photocatalytic degradation. The change in pore size and surface area is a fundamental aspect in the degradation of methylene blue (MB).

The results of magnetization measurements play a crucial role in understanding the catalytic activity of the samples under study. The magnetic behavior of a catalyst is closely related to its activity, as it can affect the reaction rate, selectivity, and stability of the catalyst [63].

Understanding the magnetic behavior of a catalyst can help to identify the factors that influence its activity and make it possible to optimize performance of the catalyst. The magnetization values changed with different resistance states and these variations can be related to with the concentration of oxygen vacancies and the conversion of the valence states of the cations. The cobalt spinel shows a paramagnetic behavior, which could be related to the magnetization value that increased with the strength of the applied magnetic field. These magnetization results provide insight into the magnetic behavior of the catalysts, which is relevant to understanding their activity. Wang et al. [64], suggest that the porosity of catalysts can play a crucial role in enhancing their catalytic activity. When an external magnetic field is applied, the magnetic force facilitates the transfer of oxygen molecules, which can reach the electroactive sites within the catalysts through the pores. Moreover, various parameters, including symmetry, structure, charge, and external field, have been found to influence the magnetic coupling between transition metal atoms, ultimately impacting catalytic activity [65].

3.9. Photodegradation mechanism

The change in radicals involved in the degradation of dye molecules occurs due to the electron (el) – hole (ho) pair and the presence of water and oxygen in the catalytic solution. The constant movement of air helps in the production of these radicals, especially hydroxyl radicals, which carry out the oxidative photodegradation of MB molecules [66]. Because the degradation of the dye involves an adsorption reaction, the adsorbed dye molecules can easily bind to the oxidizing radical species generated photocatalytically, in Fig. 12, the indicated mechanism is observed. The photodegradation of MB occurs when the surface of the catalyst is illuminated with UV light, which generates electron-hole pairs. The holes react with water molecules to form OH radicals, while the electrons are captured by O_2 to form OH- through a series of intermediate reactions involving HOO and H_2O_2, as shown in equations 1–7.

$$Co_3O_4(el^- + h^+) \rightarrow Co_3O_4(el^- + e^-)(ho^+ + ho^+) \quad (1)$$

$$ho^+ + OH^- \rightarrow OH \quad (2)$$

$$el^- + O_2^- \rightarrow O_2^- \quad (3)$$

$$H_2O + O_2 \rightarrow OOH + OH^- \quad (4)$$

$$2OOH + O_2 + H_2O_2 \quad (5)$$

$$OH + O_2 + h_{VB}^+ + MB \rightarrow \text{degrade MB} \quad (6)$$

$$OH + O_2 + h_{VB}^+ + \text{degrade MB} \rightarrow CO_2 + H_2O \quad (7)$$

4. Conclusions

The samples of $Co_{3-x}Ni_xO_4$ x = 0%, 1%, and 4% with reduced graphene oxide (rGO) were synthesized through the sol-gel method using two different routes - citric acid (R_1-CA) and cetyltrimethylammonium bromide (R_2-CTAB). The results of the analysis of the specific surface area showed that the samples with 1% and 4% Ni doping presented a larger surface area than the undoped sample, and the addition of rGO further increased this value. In particular, the 4% Ni sample with rGO had a surface area of 84.7 $m^2 \cdot g^{-1}$. The Raman studies confirmed the complete coverage of graphene by the $Co_{3-x}Ni_xO_4$ nanostructures.

The samples that showed the highest photocatalytic degradation of methylene blue (MB) were the 4% Ni doped samples obtained by R_1-CA attributed to the porous nanostructure with high specific surface area and rGO doping. The diffuse reflectance results also indicated that the

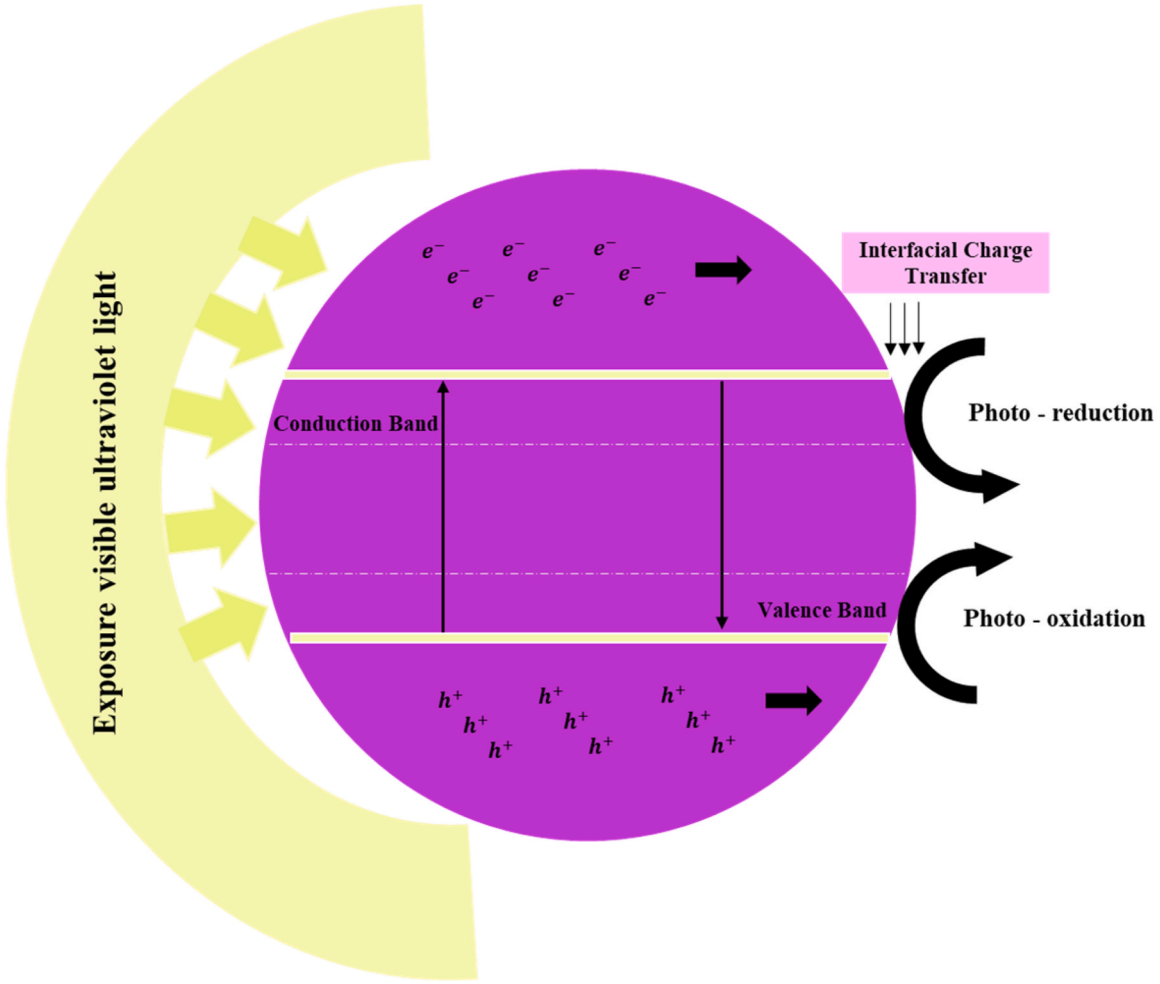

Fig. 12. Schematic representation of photocatalytic degradation in Co_3O_4 nanostructure.

band gap values of the samples obtained by R2-CTAB were lower than 1.72 eV.

CRediT authorship contribution statement

Leydi Julieta Cardenas-Flechas: Investigation, methodology & revision **Elena Xuriguera Martín**: Review, editing & resources. **Jose Antonio Padilla Sanchez**: Review & editing **Josep Ma. Chimenos Rivera**: Review, editing & resources **Miryam Rincón Joya**: Methodology, revision & supervision.

Declaration of Competing Interest

The authors declare that they have no known competing financial interests or personal relationships that could have influence the work reported in this paper.

Data availability

No data was used for the research described in the article.

Acknowledgments

The authors thank Universidad Nacional de Colombia – Campus Bogotá: Fundación Carolina-SEGIB and the Centres Científics i Tecnològics (CCiTUB) of the Universitat de Barcelona, for the support in the research stay in 2021. Thanks are due to the Catalan government for the DIOPMA (2017 SGR 118) quality accreditation awarded to their research group. This research received support from scholarships for research stays at Fundación Carolina, Madrid, Spain. Support for Research Projects, Artistic Creation and Innovation of the Universidad Nacional de Colombia-Bogotá-2020, Code: 51055, QUIPU.

References

[1] A. Akgsornpeak, T. Witoon, T. Mungcharoen, J. Limtrakul, Development of synthetic CaO sorbents via CTAB-assisted sol–gel method for CO_2 capture at high temperature, Chem. Eng. J. 237 (2014) 189–198, https://doi.org/10.1016/j.cej.2013.10.023.

[2] E.M. Jubeer, M.A. Manthrammel, M. Shkir, P.A. Subha, I.S. Yahia, S.A. Alfaify, Microwave assisted synthesis of quantum dots like ZnS nanoparticles for optoelectronic applications: An effect of CTAB concentrations, Optik 240 (2021), 166812, https://doi.org/10.1016/j.ijleo.2021.166812.

[3] M. Haneef, I.H. Gul, M. Hussain, I. Hassan, Investigation of magnetic and dielectric properties of cobalt cubic spinel ferrite nanoparticles synthesized by CTAB-assisted Co-precipitation method, J. Supercond. Nov. Magn. 34 (2021) 1467–1476, https://doi.org/10.1007/s10948-021-05869-z.

[4] S.K. Mishra, U.K. Tripathi, R.R. Awasthi, R.K. Shukla, I. Kumar, R. Mohan Naik, D. P. Mishra, CTAB mediated synthesis of ZnO nanoparticles: Structural, optical and enhanced blue-green optical emission, Mater. Today.: Proc. 46 (2021) 2229–2234, https://doi.org/10.1016/j.matpr.2021.03.481.

[5] Y. Gong, G. Liu, Q. Wang, A. Zhu, P. Liu, Q. Wu, Synthesis of a novel mesoporous Fe_3O_4@SiO_2/CTAB-SiO_2 composite material and its application in the efficient removal of bisphenol A from water, Colloid Polym. Sci. 299 (2021) 807–822, https://doi.org/10.1007/s00396-020-04801-6.

[6] Y. Wang, J.C. Shi, J.L. Cao, G. Sun, Z.Y. Zhang, Synthesis of Co3O4 nanoparticles via the CTAB-assisted method, Mater. Lett. 65 (2) (2011) 222–224, https://doi.org/10.1016/j.matlet.2010.09.090.

[7] T. Niu, B. Zhou, Z. Zhang, J. Yang, X. Ji, J. Shen, Z. Zhang, A. Du, Synthesis of monolithic TiO_2 aerogels with relatively low shrinkage and improved formability

assisted by CTAB, Front. Mater. Sci. 8 (2021), https://doi.org/10.3389/fmats.2021.67457.
[8] R.B. Khomane, A.S. Prakash, K. Ramesha, M. Sathiya, CTAB-assisted sol–gel synthesis of $Li_4Ti_5O_{12}$ and its performance as anode material for Li-ion batteries, Mater. Res. Bull. 46 (2011) 1139–1142, https://doi.org/10.1016/j.materresbull.2011.03.021.
[9] K. Duangsa, A. Tangtrakarn, C. Mongkolkachit, P. Aungkavattana, K. Moolsarn, The effect of tartaric acid and citric acid as a complexing agent on defect structure and conductivity of copper samarium Co-doped ceria prepared by a sol-gel auto-combustion method, Adv. Mater. Sci. Eng.. 5592437 (2021) (2021), https://doi.org/10.1155/2021/5592437.
[10] T. Huang, Z. Qiu, Z. Hu, X. Lu, Novel method of preparing hierarchical porous $CoFe_2O_4$ by the citric acid-assisted sol-gel auto-combustion for supercapacitors, J. Energy Storage 35 (2021), 102286, https://doi.org/10.1016/j.est.2021.102286.
[11] S. Praharaj, S.K. Venkatraman, R. Vasantharaman, S. Swamiappan, Sol-gel combustion synthesis of merwinite and its biomedical applications, Mater. Lett. 300 (2021), 130108, https://doi.org/10.1016/j.matlet.2021.130108.
[12] A. Phuruangrat, B. Kuntalue, S. Thongtem, T. Thongtem, Characterization of black-light-driven $CeVO_4$ photocatalysts synthesized by sol-gel method using citric acid as complexing agent with subsequent high temperature calcination, Russ. J. Inorg. Chem. 66 (2021) 332–339, https://doi.org/10.1134/S0036023621030128.
[13] J. Zhu, Z. Gui, From layered hydroxide compounds to labyrinth-like NiO and Co_3O_4 porous nanosheets, Mater. Chem. Phys. 118 (1) (2009) 243–248, https://doi.org/10.1016/j.matchemphys.2009.07.044.
[14] J. Wang, Y. Zhu, C. Zuo, G. Guo, Y. Xiao, W. Dai, Y. Xian, Q.: 0D/2D Co_3O_4/TiO_2 Z-Scheme heterojunction for boosted photocatalytic degradation and mechanism investigation, Appl. Catal. B Environ. 278 (2020), 119298, https://doi.org/10.1016/j.apcatb.2020.119298.
[15] Hadadian, S., Masoudpanah, S.M., Alamolhoda, S.: Solution combustion synthesis of Fe3O4 powders using mixture of CTAB and citric acid fuels. Journal of Superconductivity and Novel Magnetism, 32, 353–360 (2109). doi.org/10.1007/s10948–018-4685–9.
[16] S.M. Masoudpanah, S. Alamolhoda, Solution combustion synthesis of $LiMn_{1.5}Ni_{0.5}O_4$ powders by a mixture of fuels, Ceram. Int. 45 (17) (2019) 22849–22853, https://doi.org/10.1016/j.ceramint.2019.07.327.
[17] L.J.C. Flechas, E.X. Martín, J.A.P. Sanchez, J.M.C. Ribera, M.R. Joya, Experimental comparison of the effect of temperature on the vibrational and morphological properties of $Ni_xCo_{3-x}O_4$ nanostructures, Mater. Lett. 303 (2021), 130477, https://doi.org/10.1016/j.matlet.2021.130477.
[18] Saeed, M., Alwadai, N., Farhat, L.B., Baig, A., Nabgan, W., Iqbal, M. Co3O4-Bi2O3 heterojunction: An effective photocatalyst for photodegradation of rhodamine B dye. Arab. J. Chem. 15, (2020). doi: 103732. 10.1016/j.arabjc.2022.103732.
[19] Amalthi, P., Vijaya, J.J., Kennedy, L.J., Mustafa, A., Bououdina, M.: Magnetically recoverable Nd0. 7Ca0. 3Mn1-xNixO3 polygonal-shaped perovskite nanophotocatalysts for efficient visible-light degradation of methylene blue and tetracycline. J Phys Chem Solids. 169, 110860 (2022). doi: 10.1016/j.jpcs.2022.110860.
[20] A. Chinnathambi, Synthesis and characterization of spinel FeV_2O_4 coupled ZnO nanoplates for boosted white light photocatalysis and antibacterial applications, J. Alloy. Compd. 890 (2022), 161742, https://doi.org/10.1016/j.jallcom.2021.161742.
[21] S. Sun, S. Liang, Morphological zinc stannate: synthesis, fundamental properties and applications, J. Mater. Chem. A 5 (39) (2017) 20534–20560, https://doi.org/10.1039/C7TA06221D.
[22] S. Selvamani, S. Balamurugan, S.V. Sreenija, Facile synthesis of nanocrystalline $CuFe_2O_4$ materials by molten salt flux method, AIP Conf. Proc. 1 (2016), 050046, https://doi.org/10.1063/1.4947700.
[23] T. Wang, P. Sun, F. Liu, G. Lu, Revealing the correlation between gas selectivity and semiconductor energy band structure derived from off-stoichiometric spinel $CdGa_2O_4$, Sens. Actuators B Chem. 352 (2022), 131039, https://doi.org/10.1016/j.snb.2021.131039.
[24] X. Zeng, Z. Hou, J. Ju, L. Gao, J. Zhang, Y. Peng, The cation distributions of Zn-doped normal spinel $MgFe_2O_4$ ferrite and its magnetic properties, Materials 15 (2022) 2422, https://doi.org/10.3390/ma15072422.
[25] R.M. Mohamed, A.A. Ismail, A.S. Basaleh, H.A. Bawazir, Ease synthesis of porous Copper oxide/Cobalt oxide heterostructures for superior photodegradation of Foron Blue dye, Opt. Mater.. 124 (2022), 112000, https://doi.org/10.1016/j.optmat.2022.112000.
[26] C. Fan, X. Wu, M. Li, X. Wang, Y. Zhu, G. Fu, T. Ma, Y. Tang, Surface chemical reconstruction of hierarchical hollow inverse-spinel manganese cobalt oxide boosting oxygen evolution reaction, J. Chem. Eng. 431 (2022), 133829, https://doi.org/10.1016/j.cej.2021.133829.
[27] F.T. Alshorifi, A.A. Alswat, M.A. Mannaa, M.T. Alotaibi, S.M. El-Bahy, R.S. Salama, Facile and green synthesis of silver quantum dots immobilized onto a polymeric CTS–PEO blend for the photocatalytic degradation of p-nitrophenol, ACS Omega 6 (2021) 30432–30441, https://doi.org/10.1021/acsomega.1c03735.
[28] S.A. El-Hakam, F.T. ALShorifi, R.S. Salama, S. Gamal, W.A. El-Yazeed, A. A. Ibrahim, A.I. Ahmed, Application of nanostructured mesoporous silica/bismuth vanadate composite catalysts for the degradation of methylene blue and brilliant green, J. Mater. Res. Technol. 18 (2022) 1963–1976, https://doi.org/10.1016/j.jmrt.2022.03.067.
[29] M.A. Mannaa, K.F. Qasim, F.T. Alshorifi, S.M. El-Bahy, R.S. Salama, Role of NiO nanoparticles in enhancing structure properties of TiO_2 and its applications in photodegradation and hydrogen evolution, ACS Omega 6 (2021) 30386–30400, https://doi.org/10.1021/acsomega.1c03693.
[30] V.L.E. Siong, K.M. Lee, J.C. Juan, C.W. Lai, X.H. Tai, C.S. Khe, Removal of methylene blue dye by solvothermally reduced graphene oxide: a metal-free adsorption and photodegradation method, RSC Adv. 9 (2019) 37686–37695, https://doi.org/10.1039/C9RA05793E.
[31] A. Al Nafiey, A. Addad, B. Sieber, G. Chastanet, A. Barras, S. Szunerits, R. Boukherroub, Reduced graphene oxide decorated with Co3O4 nanoparticles (rGO-Co_3O_4) nanocomposite: a reusable catalyst for highly efficient reduction of 4-nitrophenol, and Cr (VI) and dye removal from aqueous solutions, J. Chem. Eng. 322 (2017) 375–384, https://doi.org/10.1016/j.cej.2017.04.039.
[32] Y. Zeng, J. Zhong, H. Wang, M. Fu, D. Ye, Y. Hu, Synergistic effect of tunable oxygen-vacancy defects and graphene on accelerating the photothermal degradation of methanol over Co_3O_4/rGO nanocomposites, Chem. Eng. J. 425 (2021), 131658, https://doi.org/10.1016/j.cej.2021.131658.
[33] Y. Liu, X. Zhang, Effect of calcination temperature on the morphology and electrochemical properties of Co_3O_4 for lithium-ion battery, Electrochim. Acta 54 (2009) 4180–4185, https://doi.org/10.1016/j.electacta.2009.02.060.
[34] X. He, Y. Yang, Y. Li, J. Chen, S. Yang, R. Liu, Z. Xu, Effects of structure and surface properties on the performance of ZnO towards photocatalytic degradation of methylene blue, Appl. Surf. Sci. 599 (2022), 153898, https://doi.org/10.1016/j.apsusc.2022.153898.
[35] M. Pudukudy, Z. Yaakob, B. Narayanan, A. Gopalakrishnan, S.M. Tasirin, Facile synthesis of bimodal mesoporous spinel Co_3O_4 nanomaterials and their structural properties, Superlattices Micro 64 (2013) 15–26, https://doi.org/10.1016/j.spmi.2013.09.012.
[36] T. Yao, X. Guo, S. Qin, F. Xia, Q. Li, Y. Li, Q. Chen, J. Li, D. He, Effect of rGO coating on interconnected Co_3O_4 nanosheets and improved supercapacitive behavior of Co3O4/rGO/NF architecture, Nanomicro Lett. 9 (2017) 38, https://doi.org/10.1007/s40820-017-0141-9.
[37] X. Fan, Y. Xu, C. Ma, W. He, In-situ growth of Co_3O_4 nanoparticles based on electrospray for an acetone gas sensor, J. Alloy. Compd. 854 (2021), 157234, https://doi.org/10.1016/j.jallcom.2020.157234.
[38] F. Dang, Y. Wang, L. Xu, P. Cheng, Z. Weng, T. Wang, B. Zhang, Solvent-dependent synthesis of okra-shaped Co_3O_4 for acetone gas detection at low operation temperatures. ACS Appl. Electron, Mater 3 (8) (2021) 3400–3410, https://doi.org/10.1021/acsaelm.1c00383.
[39] L.J. Cardenas-Flechas, P.T.C. Freire, E.C. Paris, L.C. Moreno, M.R. Joya, Temperature-induced structural phase transformation in samples of Co_3O_4 and $Co_{3-x}Ni_xO_4$ for CoO, Materialia 18 (2021), 101155, https://doi.org/10.1016/j.mtla.2021.101155.
[40] G. Peng, Y. He, X. Wang, Y. Cheng, H. Zhang, K. Savolainen, S. Lin, Redox activity and Nano–bio interactions determine the skin injury potential of Co_3O_4-based metal oxide nanoparticles toward Zebrafish, ACS nano 14 (4) (2020) 4166–4177, https://doi.org/10.1021/acsnano.9b08938.
[41] J.P. Picard, G. Baud, J.P. Besse, R. Chevalier, Croissance cristalline et étude structurale de Co3O4, J. Less Common Met. 75 (1) (1980) 99–104, https://doi.org/10.1016/0022-5088(80)90373-2.
[42] L.J. Cardenas Flechas, A.M. Raba Paéz, M. Rincon Joya, Synthesis and evaluation of nickel doped Co_3O_4 produced through hydrothermal technique, DYNA 87 (2020) 184–191, https://doi.org/10.15446/dyna.v87n213.84410.
[43] Z. Wang, X. Li, Z. Feng, The effect of CTAB on the citrate sol-gel process for the synthesis of sodium beta alumina nano-powders, Bull. Korean Chem. Soc. 32 (2011) 1310–1314, https://doi.org/10.5012/bkcs.2011.32.4.1310.
[44] P. Ahmadi, S. Alamolhoda, S.M. Mirkazemi, Cetyltrimethylammonium bromide (CTAB) surfactant-assisted synthesis of $BiFeO_3$ nanoparticles by sol-gel auto-combustion method, J. Supercond. Nov. Magn. 31 (2018) 3307–3314, https://doi.org/10.1007/s10948-018-4596-9.
[45] L. Sun, H. Li, L. Ren, C. Hu, Synthesis of Co_3O_4 nanostructures using a solvothermal approach, Solid State Sci. 11 (2009) 108–112, https://doi.org/10.1016/j.solidstatesciences.2008.05.013.
[46] L. Yu, A. Sun, Influence of different complexing agents on structural, morphological, and magnetic properties of Mg–Co ferrites synthesized by sol–gel auto-combustion method, J. Mater. Sci. Mater. 32 (2021) 10549–10563, https://doi.org/10.1007/s10854-021-05711-1.
[47] H. Du, W. Pu, C. Yang, Morphology control of Co_3O_4 with nickel incorporation for highly efficient oxygen evolution reaction, Appl. Surf. Sci. 541 (2021), 148221, https://doi.org/10.1016/j.apsusc.2020.148221.
[48] X. Wang, S. Lu, W. Xu, Synthesis of needle-like nanostructure composite electrode of Co_3O_4/rGO/NF for high-performance symmetric supercapacitor, Crystals 12 (2022) 664, https://doi.org/10.3390/cryst12050664.
[49] M. Mayakannan, S. Gopinath, S. Vetrivel, Synthesis and characterization of antibacterial activities nickel doped cobalt oxide nano particles, Mater. Chem. Phys. 242 (2020), 122282, https://doi.org/10.1016/j.matchemphys.2019.122282.
[50] K. Agilandeswari, A. Rubankumar, Synthesis, characterization, optical, and magnetic properties of Co3O4 nanoparticles by quick precipitation, Synth. React. Inorg. Met. 46 (2016) 502–506, https://doi.org/10.1080/15533174.2014.988807.
[51] K.J. Kim, T.Y. Koh, Cationic structure and charge transport in sol–gel-derived nickel-cobaltite thin films, J. Sol. gel Sci. Technol. 77 (2016) 528–533, https://doi.org/10.1007/s10971-015-3878-y.
[52] X. Han, Z. Huang, C. He, Q. Zhang, X. Zhang, Y. Yang, Sonochemical synthesis of Co_3O_4/graphene/Co_3O_4 sandwich architecture for high-performance supercapacitors, J. Appl. Electrochem 49 (2019) 1133–1142, https://doi.org/10.1007/s10800-019-01357-4.
[53] W. Chen, H. Shen, X. Zhu, Z. Xing, S. Zhang, Effect of citric acid on structure and photochromic properties of WO_3–TiO_2–ZnO composite films prepared by a sol–gel method, Ceram. Int.. 41 (2015) 12638–12643, https://doi.org/10.1016/j.ceramint.2015.06.093.

[54] L.J. Cardenas-Flechas, J.J. Barba-Ortega, M.R. Joya, Analysis and evaluation of structural properties of Co_3O_4 microparticles obtained at low temperature, Cerâmica 68 (2022) 52–59, https://doi.org/10.1590/0366-69132022683853152.
[55] S. Takada, M. Fujii, S. Kohiki, T. Babasaki, H. Deguchi, M. Mitome, M. Oku, Intraparticle magnetic properties of Co_3O_4 nanocrystals, Nano Lett. 1 (2001) 379–382, https://doi.org/10.1021/nl015538x.
[56] C. Yao, M. Ismail, A. Hao, S.K. Thatikonda, W. Huang, N. Qin, D. Bao, Au nanoparticles introduced to spinel Co_3O_4 thin films: Switching enhancement and magnetization modulation, J. Magn. Magn. Mater. 493 (2020), 165702, https://doi.org/10.1016/j.jmmm.2019.165702.
[57] J.O.D. Malafatti, A.J. Moreira, E.C. Paris, L.J. Cardenas Flechas, O.A.P. Pereira, M. Rincón Joya, Evaluation of Ni-doped tricobalt tetroxide with reduced graphene oxide: structural, photocatalysis, and antibacterial response, Catalysts 12 (10) (2022) 1199, https://doi.org/10.3390/catal12101199.
[58] W. Liu, R. Liu, H. Zhang, Q. Jin, Z. Song, X. Zhang, Fabrication of Co_3O_4 nanospheres and their catalytic performances for toluene oxidation: The distinct effects of morphology and oxygen species, Appl. Catal. A-Gen. 597 (2020), 117539, https://doi.org/10.1016/j.apcata.2020.117539.
[59] Z. Wang, X. Hou, J. Shen, T. Li, Supported cobalt oxide nanocrystals: morphology control and catalytic performance for styrene oxidation, RSC Adv. 6 (92) (2016) 89503–89509, https://doi.org/10.1039/C6RA21442H.
[60] J. Yang, M. Wang, S. Zhao, Y. Liu, W. Zhang, B. Wu, Q. Liu, Petal-biotemplated synthesis of two-dimensional Co_3O_4 nanosheets as photocatalyst with enhanced photocatalytic activity. Int. J. Hydrog, Energy 44 (2) (2019) 870–879, https://doi.org/10.1016/j.ijhydene.2018.11.027.
[61] M. Aadil, S. Zulfiqar, M.F. Warsi, P.O. Agboola, I. Shakir, M. Shahid, N.F. Al-Khalli, Mesoporous and macroporous Ag-doped Co_3O_4 nanosheets and their superior photo-catalytic properties under solar light irradiation, Ceram. Int. 47 (7) (2021) 9806–9817, https://doi.org/10.1016/j.ceramint.2020.12.121.
[62] C. Dong, X. Xiao, G. Chen, H. Guan, Y. Wang, Synthesis and photocatalytic degradation of methylene blue over pn junction Co_3O_4/ZnO core/shell nanorods, Mater. Chem. Phys. 155 (2015) 1–8, https://doi.org/10.1016/j.matchemphys.2015.01.033.
[63] T. Li, L. Li, W. Yang, J. Pan, R. Huang, Y. Wen, Noble-metal single atom with non-metal co-doped graphene: First-principles investigation of structures, electronic and magnetic properties, J. Magn. Magn. Mater. 170418 (2023) doi.org/10.1016/j.jmmm.2023.170418. 10.1016/j.jmmm.2023.170418.
[64] L. Wang, H. Yang, J. Yang, Y. Yang, R. Wang, S. Li, S. Ji, The effect of the internal magnetism of ferromagnetic catalysts on their catalytic activity toward oxygen reduction reaction under an external magnetic field, Ionics 22 (2016) 2195–2202, https://doi.org/10.1007/s11581-016-1746-6.
[65] L. Yu, F. Li, J. Zhao, Z. Chen, Revisiting catalytic performance of supported metal dimers for oxygen reduction reaction via magnetic coupling from first principles, Adv. Powder Technol. 1 (3) (2022), 100031, https://doi.org/10.1016/j.apmate.2022.01.004.
[66] R.S. Reena, A. Aslinjensipriya, M. Jose, S.J. Das, Investigation on structural, optical and electrical nature of pure and Cr-incorporated cobalt oxide nanoparticles prepared via co-precipitation method for photocatalytic activity of methylene blue dye, J. Mater. Sci.: Mater. Electron 31 (2020) 22057–22074, https://doi.org/10.1016/j.matchemphys.2019.122282.